Royal Astronomical Society

### A PAH deficit in the starburst core of a distant spiral galaxy

Zhaoxuan Liu , 1,2,3,4\* John D. Silverman, 1,2,3,5 Emanuele Daddi , 4 Boris S. Kalita , 1,3,6†

Annagrazia Puglisi , 7‡ Qinyue Fei, 1,6,8 Alvio Renzini , 9 Daichi Kashino, 10 Francesco Valentino , 11,112

Jeyhan S. Kartaltepe, 13 Daizhong Liu , 14 Pablo G. Pérez-González, 15 Jed McKinney, 16§ Caitlin

M. Casey, 17,11 Xuheng Ding, 17 Andreas Faisst, 18 Maximilien Franco, 16 Darshan Kakkad , 19 Anton

M. Koekemoer , 20 Erini Lambrides, 21 Steven Gillman , 11,22 Ghassem Gozaliasl , 23,24 Henry

Joy McCracken, 25 Jason Rhodes, 26 Brant E. Robertson, 27 Giulia Rodighiero , 9,28 Wiphu Rujopakarn, 29,30

Tomoko L. Suzuki , 1,3 Takumi S. Tanaka , 1,2,3 Brittany N. Vanderhoof , 20 Aswin P. Vijayan, 31 Olivia

R. Cooper, 16 | Aidan Kaminsky, 32 Georgios E. Magdis , 11,22,12 and Namrata Roy , 15

Affiliations are listed at the end of the paper

Accepted 2025 July 24. Received 2025 July 24; in original form 2025 January 13

### **ABSTRACT**

We present high-resolution and spatially matched observations with JWST and ALMA of a starburst galaxy (PACS-830) at z=1.46. The NIRCam observations mainly trace the stellar light while the CO (J=5-4) observations map the dense molecular gas at kpc scales. Both data sets reveal the morphology to be that of a gas/dust-rich bulge with two extending arms, together resembling a grand-design spiral galaxy. The more pronounced arm contributes  $21 \pm 6$  per cent of the total CO emission. These results demonstrate that starburst activity at high redshift can be triggered, without undergoing a highly disruptive major merger. We assess the strength and distribution of star formation using two tracers: (1) polycyclic aromatic hydrocarbons (PAHs) emission detected at 8  $\mu$ m ( $L_8$ ) with a MIRI/F1800W image, and (2)  $L_{\rm IR}$ , inferred from the CO (J=5-4) map. The spatial profiles of the  $L_{\rm IR}$  and  $L_8$  are dissimilar, thus leading to a significant deficit of mid-IR ( $L_8$ ) emission in the nucleus. We hypothesize that this is due to the destruction of PAH molecules by the intense ionizing radiation field or decreased emission in the photodissociation region, as seen in nearby star-forming regions and consistent with the galaxy-wide properties of distant starbursts. This study reveals spatial variations in the  $L_8$  to  $L_{\rm IR}$  ratio for the first time at z>1, in agreement with expectations from theory. Our analysis underscores the pivotal role of joint high-resolution observations with JWST and ALMA in discerning the different phases of the interstellar medium and revealing internal physics in galaxy substructures.

Key words: galaxies: high-redshift - galaxies: spiral - galaxies: starburst - galaxies: star formation.

### 1 INTRODUCTION

Cosmic noon (1 < z < 3), the epoch during which global star formation peaks across cosmic time (Madau & Dickinson 2014; Tacconi, Genzel & Sternberg 2020), is crucial for star-forming galaxies (SFGs) as they develop their internal structure, particularly the bulge (e.g. Tan et al. 2024a). A key distinction between SFGs at this epoch and those in the local Universe is their abundant gas content (Tacconi et al. 2013), which likely leads to an increased star formation efficiency (SFE), i.e. the star formation rate (SFR) per unit gas mass.

\* E-mail: zhaoxuan.liu@ipmu.jp

† Joint-Kavli Astrophysics Fellow.

‡ Anniversary Fellow.

§ NASA Hubble Fellow.

|| NSF Graduate Research Fellow.

© The Author(s) 2025.

Within the star-forming population even at high-z, the starbursts are rapidly building the bulk of their stellar mass and standing out as significant outliers (> 0.3 dex) with elevated SFRs compared to typical 'main sequence' (MS) galaxies, which is defined by the tight correlation between SFR and stellar mass (Daddi et al. 2007) observed up to  $z \sim 10$  (Calabrò et al. 2024). Such intense star formation is associated with dust enrichment and subsequent attenuation of UV/optical light thus requiring tracers of star formation that can penetrate the heavily obscured regions of galaxies.

At submillimeter wavelengths, starburst galaxies exhibit strong emission lines (e.g. CO and C) and dust continuum, which effectively traces not only star formation activity, less hampered by dust attenuation, but also gas kinematics. Evidently, ALMA is effective at unveiling the nature of starbursts; for instance, kpc-scale studies reveal that many high-z starbursts are rotation-supported discs (Hodge et al. 2016; Cowie et al. 2018; Gullberg et al. 2019; Hodge & da Cunha 2020; Rizzo et al. 2023), contrasting with their local analogues, which are predominantly triggered by highly disruptive

major mergers. Even for extreme starbursts like hyperluminous infrared galaxies ( $L_{\rm IR} > 10^{13}\,{\rm L}_{\odot}$ ), recent hundred-parsec ALMA studies have found a massive rotating disc at z=2.3 instead of major merger origin (Liu et al. 2024a). This growing number of rotationally supported starbursts suggests that secular evolution with *in situ* disc instabilities may be sufficient to drive high levels of star formation (see Förster Schreiber & Wuyts 2020, for a review). However, before the advent of *JWST*, the limited infrared (IR) capabilities of the last generation of telescopes, e.g. *HST*, did not allow for spatially resolved analysis of the stellar counterpart for these rotating discs due to the strong attenuation by dust.

Now with *JWST*, the full scale of stellar morphology at z>1 is being revealed, complete with spiral arms, clumps, and bulges as seen by high resolution and deep NIRCam observations (e.g. Rujopakarn et al. 2023; Liu et al. 2024b; Kalita et al. 2024, 2025a,c; McKinney et al. 2025). In fact, massive galaxies, previously classified as mergers, are now being found to be more typical and disc-like with spiral arms and clumps surrounding bright, compact sub-mm sources emitted from their dust-obscured centers, likely bulges in formation (Hodge et al. 2016, 2019; Polletta et al. 2024; Liu et al. 2024b; Tan et al. 2024a).

Another diagnostic opportunity now offered by JWST concerns; the resolved imaging and spectroscopy covering polycyclic aromatic hydrocarbons (PAHs) emissions (e.g. Alberts et al. 2024; Shivaei & Boogaard 2024; Shivaei et al. 2024). PAHs are key constituents of interstellar dust in galaxies (Draine & Li 2007). The emission lines of PAHs, spanning the rest-frame infrared spectrum of 3-20 μm, serve as efficient coolants and dominate the mid-IR luminosity for high SFR galaxies with little active galactic nucleus (AGN) contribution (Draine 2003: Tielens 2008: Li 2020, and references therein). Though the attenuation can be non-zero across the mid-IR, PAH features, especially the dominating 7.7 µm line, are less affected by dust obscuration, compared to the traditional H  $\alpha$  tracer for dusty, distant SFGs (Lai et al. 2020, 2024). Consequently, PAH emissions are utilized to trace SFRs in normal, SFGs due to their prevalence in star-forming regions illuminated by ultraviolet (UV) photons from young stars (e.g. Calzetti 2013; Chastenet et al. 2023; Dale et al. 2023; Lee et al. 2023; Ronayne et al. 2024).

While PAH features exhibit a tight correlation with galaxy-wide SFR, whether they are reliable tracers of spatially resolved star formation is still under investigation. For example, PAH molecules can be dissociated by UV photons from star formation or AGN accretion disc as shown by theory (Leger et al. 1989). Using the Spitzer Space Telescope, many studies have reported a deficit of PAH emission in the cores of AGNs or compact starbursts based on infrared spectrograph (IRS) spectroscopy (e.g. Desai et al. 2007; Díaz-Santos et al. 2011; Stierwalt et al. 2013, 2014; Zhang, Ho & Li 2022). Inami et al. (2013) also present similar observations in a survey of 202 local luminous infrared galaxies via the AKARI telescope. Recently, studies using mid-infrared instrument imaging (MIRI) aboard JWST have found evidence of PAH deficits in H II regions in nearby AGNs (e.g. Lai et al. 2022, 2023) and even in normal SFGs (e.g. Egorov et al. 2023; Spilker et al. 2023; Pedrini et al. 2024; Battisti et al. 2025). Therefore, such deficits could also occur due to strong radiation fields in star-forming regions and their effects should be considered when utilizing PAH emissions to infer SFRs.

In the distant Universe, such deficits are linked to a high SFR density ( $\Sigma_{SFR}$ ) and starburstiness ( $R_{SB} = SFR/SFR_{MS}$ ), shown by an empirical relationship established between the global total infrared luminosity  $L_{IR}$  and PAH emission at rest-frame 8  $\mu$ m  $L_8$  up to  $z \sim 2.5$  (Elbaz et al. 2011, 2018). Such trends are further confirmed

by spectroscopic studies using Spitzer (e.g. Pope et al. 2013; McKinney et al. 2020). With *JWST*, MIRI can now provide unparalleled sensitivity and spatial resolution at mid-infrared wavelengths, making resolved studies of galaxies in the distant Universe feasible (Magnelli et al. 2023; Alberts et al. 2024; Lyu et al. 2024; Ronayne et al. 2024; Shivaei et al. 2024).

Here, we report a spatially resolved study of a starburst galaxy at z=1.463, PACS-830, with clear spiral morphology and potential bulge in formation, to compare star-forming conditions across the surface of the galaxy. In Section 2, we introduce our multiwavelength observations with HST, JWST, and ALMA. We integrate these data sets to model the dust-obscured stellar mass distribution on a pixel-by-pixel basis using HST and JWST/NIRCam images and to compare the distribution of two SFR tracers, the PAH emissions from JWST/MIRI observations with ALMA CO (J=5-4) data. In Section 3, we detail this modelling process. In Section 4, we analyse the results in terms of galaxy morphology and the variation of  $L_{IR}/L_8$ . In this work, we adopt a Chabrier (2003) IMF and the standard  $\Lambda$ CDM model with  $H_0=70~{\rm km~s}^{-1}{\rm Mpc}^{-1}$ ,  $\Omega_{\Lambda}=0.7$ ,  $\Omega_{\rm M}=0.3$ .

### 2 OBSERVATIONS OF PACS-830

PACS-830 (J2000 RA = 10:00:08.7462, Dec. = +02:19:01.876) is a starburst galaxy, identified by Herschel/PACS photometry (Rodighiero et al. 2011). SED fitting, based on photometry from UV to radio, including measurements from Herschel, places this galaxy as a moderate starburst,  $4\times$  above the MS at z=1.463 (fig. 1 in Silverman et al. 2015). With accurate redshift estimation through spectroscopic observations with Subaru Telescope as part of the FMOS-COSMOS survey (Kashino et al. 2019), the total SFR in PACS-830 is estimated to be  $412^{+62}_{-54}$  M<sub> $_{\odot}$ </sub> yr<sup>-1</sup>, derived from its infrared luminosity  $L_{\rm IR}$  (Silverman et al. 2018a). Stellar mass ( $M_*$ ) estimation using global multiwavelength photometry by Liu et al. (2021) finds  $M_* = 10^{11.04}$  M<sub> $_{\odot}$ </sub>.

PACS-830 shows no evidence of an AGN. The BPT diagram analysis by Silverman et al. (2015) with FMOS spectra confirms that PACS-830 lies within the star-forming region. The galaxy shows no detection in previous X-ray surveys with *Chandra* and *XMM-Newton* in the COSMOS field (Cappelluti et al. 2009; Civano et al. 2016; Marchesi et al. 2016). Further, Liu et al. (2021) conducted SED fitting with 11 bands from Mid-IR to radio using both CIGALE (Boquien et al. 2019) and MICHI2 (Liu et al. 2019) and found an insignificant AGN contribution.

### 2.1 High-resolution ALMA observations

PACS-830 was observed with ALMA Band 6 during a Cycle 4 program (Proposal #2016.1.01426.S; PI J. Silverman), to map the molecular gas distribution in three starbursts at  $z \sim 1.5$ . The onsource times with extended (47 antennas) and compact (43 antennas) configurations were 70.6 and 11.9 minutes, respectively. The native spectral resolution is 5.022 km s<sup>-1</sup>.

We recalibrated the data by running the Common Astronomy Software Applications (CASA) standard pipelines and co-add the data from the extended and compact configurations to create a data cube with high dynamic range. Before constructing the images, we first measured the centroid and full width at half maximum (FWHM) of CO (J=5-4) line from the high-resolution data cube provided as a part of the QA2 products from ALMA. After flagging a spectral region of 4 × FWHM (305 km s<sup>-1</sup>) centred at 233.96 GHz (line centroid), the continuum was imaged with the *tclean* algorithm in multifrequency synthesis (mfs; Conway, Cornwell & Wilkinson

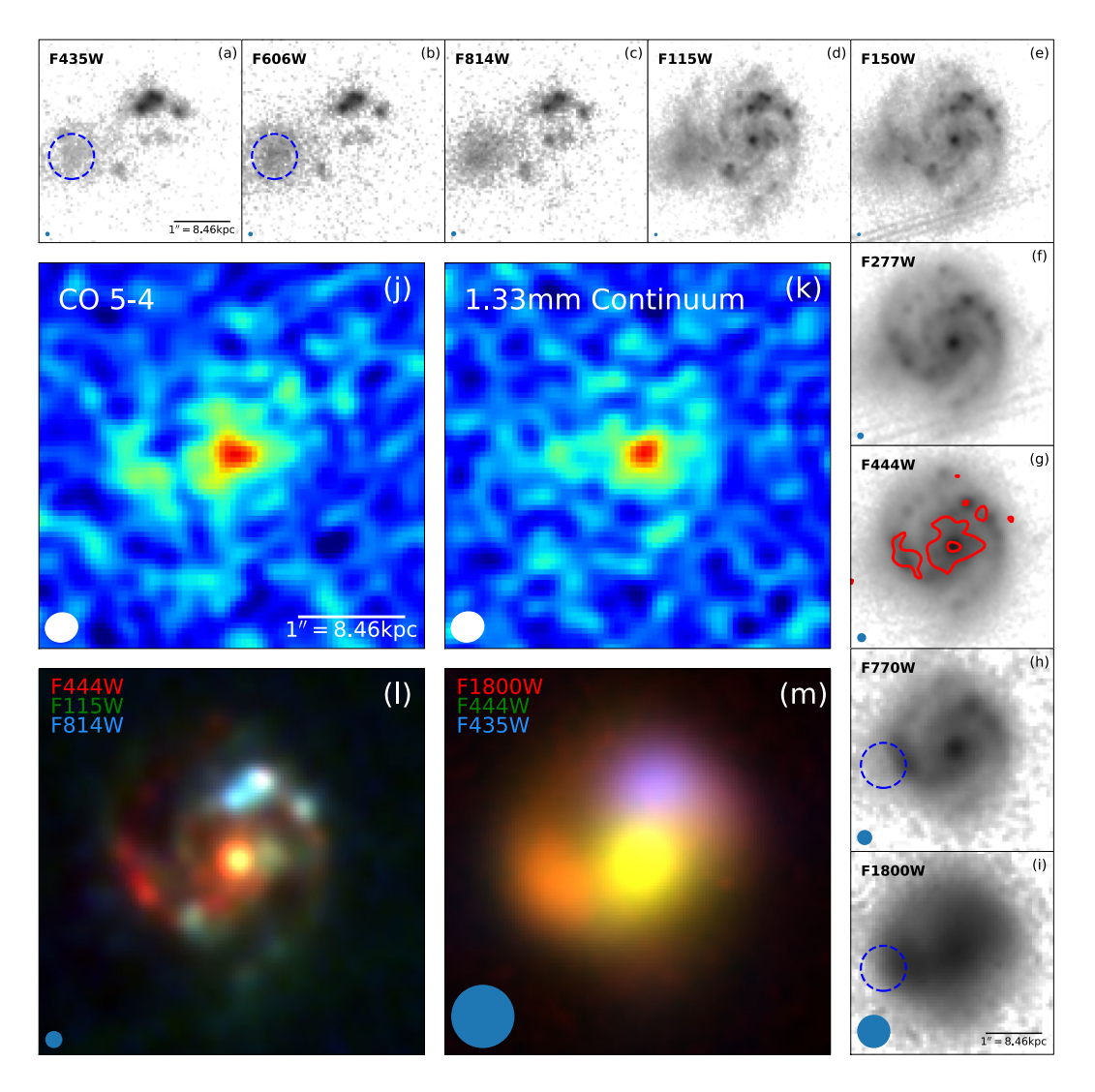


**Figure 1.** Observations of PACS-830. The surrounding panels show images of different instrument/filter combinations: (a) *HST F435W*, (b) *HST F606W*, (c) *HST F814W*, (d) *JWST/*NIRCam *F115W*, (e) *F150W*, (f) *F277W*, (g) *F444W*, and (h) MIRI *F770W*, and (i) *F1800W* images. ALMA observations of PACS-830 are shown in the larger upper panels (j: CO 5–4, k: 1.33-mm continuum). All panels span the same region of the sky, with north at the top and east to the left. The PSF of each filter is shown in the lower-left corner of each panel. The physical scale of 1 arcsec is 8.46 kpc, as indicated in the lower-right corner in panels a, i, and j. The bottom two panels in the middle are two RGB images generated by the filter pairs: *F444W*, *F115W*, and *F814W* (rest-frame NIR + optical + UV, l) and *F1800W*, *F444W*, *F435W* (PAH + stellar mass + unobscured SFR, m), respectively, after subtracting the foreground galaxy and being convolved to the widest PSF within the pair (see Section 3.1). The position of the foreground galaxy is highlighted with dashed circles in the panels a–b and h–i. We highlight the emergence of clumpy spiral features at longer wavelengths in the *JWST* images, which aligns with the CO (J=5-4) contours shown in panel g. These contours are plotted at levels of 3 and 9 ×  $\sigma_{rms}$ , where  $\sigma_{rms} = 0.029$  Jy beam<sup>-1</sup> km s<sup>-1</sup>.

1990) mode using the rest channels from 215 to 235 GHz (Fig. 1k). We then subtracted the continuum from the visibilities using *uvcontsub*. For the CO (J=5–4) intensity map (Fig. 1j), we adopted the method outlined in Akins et al. (2022), i.e. running *tclean* in the *mfs* mode over a frequency range covering the emission line to derive a pseudo-moment 0 map. The frequency range of the combined channels is  $2\times FWHM$  centred at the line centroid. This approach increased the signal-to-noise ratio (S/N) and ensured the detection of the faint and diffuse emission of the ISM in PACS-830 as it stacks the channels prior to *tclean*. For both images, we utilized *auto-multithresh* to create masks for cleaning with the threshold parameters for extended configurations suggested in Kepley et al. (2020), together with a *multiscale* (Cornwell 2008) deconvolver to recover the extended emissions. We opted for robust Briggs weighting (0.5; Briggs 1995) to balance the S/N and spatial

resolution. We first created the dirty images without cleaning to measure the  $\sigma_{rms}$  and then cleaned the images to  $0.5 \times \sigma_{rms}$ . The resulting restored beams are  $0''.31 \times 0''.28$  and  $0''.31 \times 0''.27$ . We use CASA 4.7.2, as specified in the QA2 report, to carry out the recalibration of the raw data. The imaging, measurements, and analysis, are processed by CASA 6.2.1.

### 2.2 JWST and HST observations

With PACS-830 located in the COSMOS field, it is covered by two *JWST* Cycle 1 programs: COSMOS-Web (PIs: Casey & Kartaltepe; Casey et al. 2023; GO #1727) and PRIMER (PI: Dunlop; Dunlop et al. 2021; GO #1837). PACS-830 was observed with four NIRCam filters (F115W, F150W, F277W, F444W;  $5\sigma$  depths: 27.13, 27.35, 27.99, 27.83 mag) and one MIRI filter (F770W;  $5\sigma$  depth: 25.4 mag)

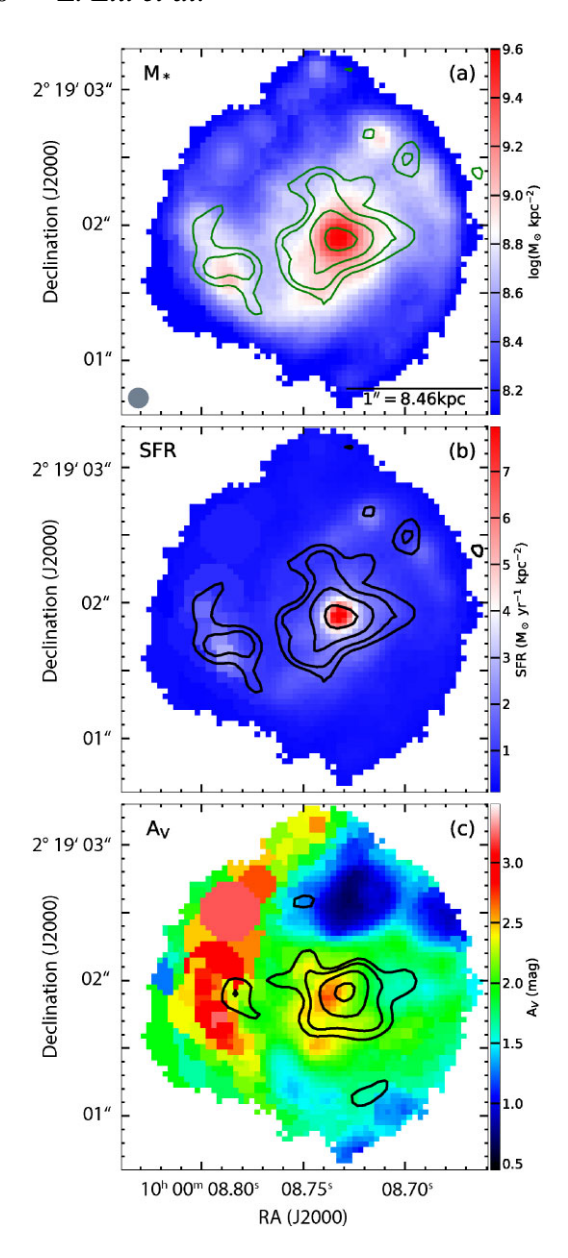


**Figure 2.** Spatially resolved SED fitting: stellar mass (a), SFR (b), and dust extinction (c). CO (J=5–4) contours are overlaid in panels a and b for comparison. In panel c, dust continuum contours are shown for comparison with the dust attenuation. Contours for the CO emission are plotted at levels of 3, 4, 6, and  $9 \times \sigma_{\rm rms}$ . Contours for the dust continuum are at the same levels, with  $\sigma_{\rm rms} = 0.01$  mJy beam<sup>-1</sup>. The physical scale, 1'' = 8.46 kpc, is shown in the lower-right corner of panel a.

by COSMOS-Web and additional MIRI filters (F770W and F1800W;  $5\sigma$  depths: 26.0 and 23.0 mag) by PRIMER. Since the detector angles differ between the two programs, we are unable to stack the F770W observations. Consequently, we use the PRIMER data set for MIRI imaging observations, as it offers more depth compared to the COSMOS-Web survey. The NIRCam images were recalibrated and produced by the COSMOS-Web team (Franco et al. 2025) and the data reduction of the MIRI images from the PRIMER team is detailed in Pérez-González et al. (2024). The NIRCam images (Figs 1d–g) are all reduced to a spatial scale of 30 mas pixel $^{-1}$  while the MIRI ones (Figs 1h–i) are in 60 mas pixel $^{-1}$ .

We also include rest-frame UV imaging from archival *HST*/ACS observations in filters *F*435*W*, *F*606*W*, and *F*814*W*, where much of this data come from the original COSMOS *HST* (Koekemoer et al. 2007), and the CANDELS survey (Grogin et al. 2011; Koekemoer et al. 2011), in addition to other archival programs. These images (Figs 1a–c) were retrieved from the DAWN *JWST* Archive (DJA)¹ and reduced to 40 mas pixel⁻¹ using grizli software (Brammer 2023).

With images from *HST*, *JWST*/NIRCam, *JWST*/MIRI, and ALMA, we have gathered a comprehensive data set of multiwavelength observations for PACS-830. These observations, ranging from restframe UV and optical to NIR, MIR, and FIR, offer a detailed, spatially resolved view of a high-*z* starburst galaxy. This approach allows us to dissect its complex morphology and physical properties. PACS-830 is similar to our study of another starburst galaxy from the same sample, PACS-819 (11× MS, as detailed in Liu et al. 2024b), where we ruled out the major-merger scenario as the trigger for its starburst activity, despite PACS-819 having a clumpy morphology in the *HST* observations at rest-frame UV.

### 3 IMAGE MODELLING

### 3.1 Pixel-by-pixel SED fitting

Using the HST and JWST/NIRCam images, we conducted pixel-bypixel SED fitting (Fig. 2) to discern the stellar mass distribution and the magnitudes of the dust attenuation for this complex starburst system. First, we detected a foreground galaxy<sup>2</sup> to the east which slightly overlaps with PACS-830 (Fig. 1a), next to the spiral arm. We subtracted this foreground galaxy using Galight (Ding et al. 2020) in filters bluer than F277W, where the foreground galaxy contributes significantly. We modelled the whole field of view of F606W, where PACS-830 and the foreground galaxy have the best contrast. Then, we fixed the shape and position of the foreground galaxy when modelling the galaxies in other filters and subtracted the foreground component from the original images. The PSF of HST images are based on field stars auto-detected by Galight while the JWST PSFs are generated using PSFEx (Bertin 2011) and provided by Tanaka et al. (2025). The fitting result of F606W is shown in Fig. A1 as an example of this exercise.

The foreground subtracted images, F277W and F444W images are used to construct the pixel-by-pixel SED model following the same procedures as in Liu et al. (2024b). The wavelength coverage is from rest-frame UV 1650 Å to near-IR 1.8 µm. We construct a binned flux cube with a spatial scale of 40 mas pixel<sup>-1</sup> and FWHM matching the F444W PSF (0.16 arcsec) using piXedfit\_bin in pixedfit (Abdurro'uf et al. 2021). When binning, we required all bins with similar SED shapes to have an S/N > 3 in JWST bands. Before fitting, the bins containing the PSF spikes shown in Figs 1(e)– (f) are manually masked. When running SED fitting pixel-by-pixel with bagpipes (Carnall et al. 2018), we used the setting in Liu et al. (2024b) designed for another starburst at a similar redshift to fit a constant SFH model with the solar metallicity. Fig. 2 shows the stellar mass map (a), SFR map (b), and dust attenuation map (c) from the pixel-by-pixel SED fitting. We used the F277W image as a reference to redistribute the SED-based stellar mass from each

<sup>&</sup>lt;sup>1</sup>https://dawn-cph.github.io/dja/index.html

<sup>&</sup>lt;sup>2</sup>Based on the Lyman break wavelength determined using GALEX, we conclude this galaxy has a redshift below 0.5, in agreement with the estimated photo-*z* in the COSMOS catalogues (Capak et al. 2007; Ilbert et al. 2009).

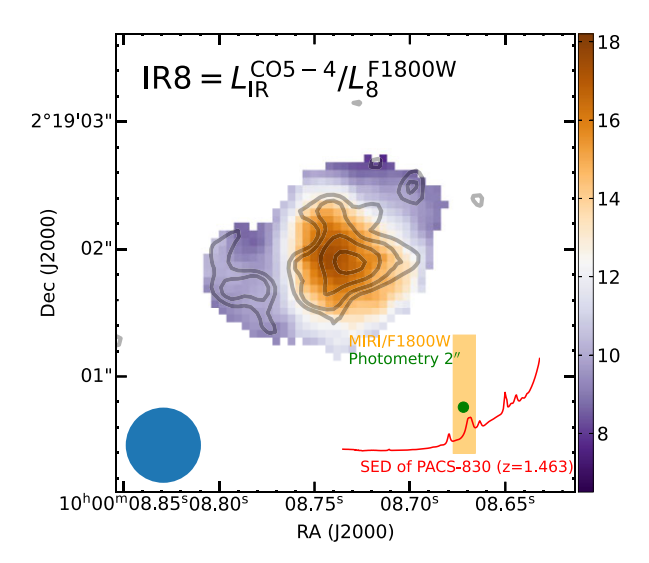


**Figure 3.** Spatially resolved IR8 map of PACS-830. The PSF of F1800W is shown in the lower-left corner. CO J=5–4 contours are overlaid for comparison, highlighting regions of the dense molecular gas. The figure shows the same field of view as Fig. 1. The subpanel in the lower-right corner demonstrates the modelled spectral energy distribution (SED) of the PAH emission of PACS-830, as detailed in Liu et al. (2021). The F1800W aperture photometry (r = 2''; filled circle) aligns well with the SED.

spatial bin to individual pixels, assuming that stellar mass linearly scales with the F277W flux within the same bin. This allows us to create a higher-resolution stellar mass map, leveraging the fact that the F277W band (rest-frame 1.1  $\mu$ m) closely traces the stellar light distribution.

### 3.2 Spatially resolved IR8 map

Elbaz et al. (2011) used Spitzer photometry at the rest-frame 8  $\mu$ m for SFGs up to z=2.5 to determine the contribution of PAH 7.7  $\mu$ m emission to the total infrared luminosity. Despite the drawback of not removing the continuum, the dominant PAH 7.7  $\mu$ m emission still established a tight empirical relationship between the luminosity at 8  $\mu$ m ( $L_8$ ) and the total infrared luminosity ( $L_{\rm IR}$ ).

Thanks to the high sensitivity and resolution of ALMA and JWST, we can investigate this relationship on a spatially resolved manner. The F1800W filter covers the rest-frame wavelength of 8 µm of PACS-830, as shown in Fig. 3. This allows us to use the flux in F1800W as a spatially resolved proxy for  $L_8$  at 0.59'' resolution. To account for the difference between the flux in F1800W and IRAC-8 μm passband, we apply a k-correction using the SED template of M82 from Polletta et al. (2007) to make a fair comparison with the results in Elbaz et al. (2011). The corrected flux is 1.3 times lower. We infer the spatially resolved  $L_8$  map from the F1800W image by converting the corrected flux to luminosity. To assess the spatially resolved  $L_{IR}$ , we utilize high-resolution ALMA observations of CO (J=5-4) instead of the dust continuum. This approach avoids the extra uncertainty introduced by temperature variations in the dust component, as CO (J=5-4) flux is independent of dust modelling, allowing us to infer  $L_{\rm IR}$  in each pixel at 0.3 arcsec resolution. The conversion is based on the empirical linear relation between CO (J=5-4) luminosity  $L'_{CO[5-4]}$  and the total infrared luminosity  $L_{IR}$ , well demonstrated in Greve et al. (2014), Daddi et al. (2015), Liu et al. (2015), and Valentino et al. (2020). We adopt the equation in

Daddi et al. (2015), as follows:

$$\log L_{\rm TIR}/L_{\odot} = \log L'_{\rm CO[5-4]}/({\rm K~km~s^{-1}~pc^{2}}) + 2.52, \tag{1}$$

where  $\log L'_{\text{CO[5-4]}}$  is calculated using equation (1) in Solomon & Bout (2005).

By dividing the  $L_{\rm IR}$  map by the  $L_8$  map, we derive the spatially resolved IR8 ( $\equiv L_{\rm IR}/L_8$ ) map shown in Fig. 3, which indicates the PAH contribution to the total infrared luminosity. Prior to dividing these maps, the  $L_{\rm IR}$  map is convolved with a Gaussian kernel to match the FWHM of the PSF of F1800W (0.59 arcsec, see Section 3.3 for details), and the region with a CO S/N lower than 4 is masked. Applying the same mask on the F1800W image, the remaining pixels have an S/N higher than 30. The  $L_{\rm IR}$  map is also regridded to the image of F1800W. The uncertainty in each pixel of the IR8 map is dominated by the 0.2 dex uncertainty in equation (1). The systematic uncertainty of imaging processing is minimal and it does not affect the conclusions in the following sections, as the astrometry offset remains below one pixel, while the F1800W point spread function (PSF) is about 10 times larger than the pixel scale (60 mas).

### 3.3 Sérsic model fitting

Two-dimensional modelling of the galaxy morphology using Sérsic models allows for a precise quantitative analysis of the distribution of galaxy emissions while mitigating the impact of PSF smearing (e.g. see Magnelli et al. 2023 for attempts with MIRI images). Here, we employ Sérsic fitting to analyze the distribution of the PAH emissions in F1800W using Galight (Ding et al. 2020).

We utilize WebbPSF (Perrin et al. 2012) to model the PSF of F1800W, given the observation configuration (e.g. observation date, integration time, and position angle). It is an alternative method since we fail to generate an empirical PSF due to the absence of adequate stars in the field of view. We first attempted to fit the entire galaxy with a single Sérsic component, but this resulted in significant residuals in the spiral arm regions to the east and north, which are cospatial with the red and blue regions in the RGB Fig. 1(m). The construction of the RGB images is detailed in the following section. To better account for the galaxy's structure, we performed model fitting with three components: a central Sérsic to represent the unresolved core, and two additional Sérsic components representing the spiral arms to the east and north. These arms exhibit considerable star formation activity, as traced by CO and UV emission, and they also peak in PAH emission. Modelling them separately improves the fit and reduces residuals in these regions. The model is optimized with a Particle Swarm Optimizer (PSO; Kennedy & Eberhart 1995). The best-fitting Sérsic index (n) of the central component is 0.98, with an effective radius  $R_e$  of 0.49 arcsec. The effective radius  $R_e$  is calculated as the half-light radius.

### 3.4 Spergel model fitting

ALMA measures visibilities in the uv-plane instead of acquiring direct images. The structure in the reconstructed images is composed of noise and Gaussian created by the cleaning process, which is affected by the weighting scheme and the configurations for cleaning. Therefore, to accurately assess the morphology of CO (J=5–4), we fit the visibilities of the emission line in the uv-plane with a Spergel model (Spergel 2010) using GILDAS. In uv-space, the Spergel model provides a good approximation of the Sérsic profile which lacks analytical Fourier transformability (Tan et al. 2024b). The fitted result for  $R_e$  is  $0.51\pm0.02$  arcsec, similar to the result based on the F1800W image. The Spergel index v is estimated to be  $-0.2\pm0.1$ . Using the

fitted  $\nu$ , radius and beam size of CO (J=5–4), we derive a Sérsic index of 1.7±0.2, converted from  $\nu$  using the equation (3) in Tan et al. (2024b).

### 4 RESULTS

### 4.1 The multiwavelength morphology of PACS-830

The multiwavelength observations of PACS-830 (Fig. 1) depict a morphological transition from a major-merger-like structure in the rest-frame UV to a face-on, grand-design spiral galaxy with two well-formed arms in the mid-IR. As revealed by *JWST*, similar wavelength-dependent changes in morphology have been seen in starbursts at cosmic noon and other dusty SFGs, due to high dust attenuation in central star-forming regions (e.g. Ferreira et al. 2023; Kokorev et al. 2023; Bail et al. 2024; Gillman et al. 2024; Polletta et al. 2024; Liu et al. 2024b; Faisst et al. 2025).

To indicate variations in morphology with wavelength (e.g. Bail et al. 2024), we created RGB images from two sets of *JWST* images after subtracting the foreground galaxies. The colour image in Fig. 1(1) uses *F*814*W*, *F*115*W*, and *F*444*W* to indicate the blue (rest-frame UV, tracing the unobscured stars), green (rest-frame optical), and red (rest-frame near-infrared, tracing the obscured stellar population) components. The second colour image (Fig. 1m) uses *F*435*W*, *F*444*W*, and *F*1800*W* thus presenting the blue (rest-frame UV, tracing the unobscured stars), green (rest-frame near-infrared, tracing the obscured stellar population), and red (rest-frame mid-infrared, PAH emissions) components. Before combining, the images are matched in resolution to the image with the widest PSF, which are *F*444*W* (0.16 arcsec) and *F*1800*W* (0.59 arcsec) for the two sets, respectively.

As shown in Fig. 1(1), the morphology of the starburst consists of a dusty starburst core, resembling a galactic bulge, along with many bright knots distributed along two evident spiral arms. There are faint (spiral) features connecting these components, which remain below the detection threshold in *HST* images. The RGB images (Figs 1(1 and m)) reveal that the clumps, mainly along the arms, vary in colour, thus likely have different ISM conditions. Among these clumps are two particularly notable regions: one to the north of the central core, which is UV bright, and another to the east, which shows strong dust attenuation. The clumps near the central core may contribute to the formation of the galaxy's bulge.

We emphasize that the CO (J=5-4) emission distinctly reveals the spiral arms,<sup>3</sup> with notably clearer detection in the eastern arm. We highlight this by overlaying the CO (J=5-4) contours on the F444W image, which traces the stellar component (Fig. 1g). We fit the CO (J=5-4) emission of the eastern arm and the core simultaneously with two Gaussian models using the Cube Analysis and Rendering Tool for Astronomy (CARTA; Comrie et al. 2021) and find the flux contribution of the arm to the total is  $21\pm6$  per cent.

The dense gas in the southeastern spiral arm appears highly extended in Fig. 1(j), which could result from two bright clumps being blended into a single structure – consistent with how the two clumps in Fig. 1(f) appear merged in Fig. 1(h). To assess the impact of resolution, we degraded the *F277W* image to the *F770W* resolution via PSF matching. The resulting flux ratio map shows no clear evidence for multiple clumps in the arms or bulge, indicating that the extended appearance in *F770W* is largely due to resolution-induced blending.

As shown in Figs 1(j) and (k), the bulk of star formation, as indicated by CO and continuum emission, is concentrated in the galactic center, suggesting the presence of a bulge in formation, a feature commonly observed at cosmic noon (e.g. Jiménez-Andrade et al. 2019; Tan et al. 2024a). The slightly distorted morphology of the starburst core in CO(J=5-4) may similarly arise from limited resolution and sensitivity, as clumps and bulge structures, distinguishable by colour in the RGB image (Fig. 1(1)), could become spatially blended.

The stellar mass map (Fig. 2a) clearly shows the spiral arms, where the stellar mass surface density  $\Sigma_{M_*}$  is roughly double that of the off-arm regions of the disc. In the central region,  $\Sigma_{M_*}$  peaks at  $10^{9.6}\,M_{\odot}$  kpc<sup>-2</sup> – about 25 times higher than the off-arm regions and 10 times higher than the arms – indicating a bulge. Though the eastern arm is slightly more massive than the western one, indicating a slight asymmetry in the morphology, the mass distribution shows no evidence of a major merger triggering the starburst.

The SFR map (Fig. 2) from pixel-by-pixel SED fitting based on the HST and NIRCam images shows regions of enhanced star-forming activity, i.e. the galactic core and the spiral arm to the east. These sites of enhanced SF activity are also co-spatial with the peaks in CO (J=5-4).

The  $A_V$  map reveals that the difference in dust attenuation between the northern UV emitting part and the central part is two magnitudes, resulting in the merger-like morphology in the rest-frame UV. The part with the highest dust attenuation resides in the eastern spiral arm. It aligns with the fact that the eastern arm is much fainter in the rest-frame optical (Figs 1d and e) but becomes comparably bright in the rest-frame NIR (Figs 1g and h). However, the dust continuum does not peak here: it is in its close vicinity, as shown in Fig. 2(b). This could simply be a result of a low signal-to-noise ratio (SNR) of the dust continuum. Consequently, we are reluctant to use the dust continuum to infer the molecular gas distribution as in Liu et al. (2024b) or include it in the pixel-by-pixel SED fitting. A deeper and higher resolution observation is necessary to address this question, which is beyond the scope of the current data set. The mismatch in the core region could be an effect of convolution as, after convolving the bluer bands to the coarse PSF, the light from the blue clumps to the west of the core may contaminate the flux in the center, thus leading to a slightly lower A<sub>V</sub>.

## 4.2 An IR8 enhancement in the core: a PAH deficit in the starbursting core?

IR8 is defined as the ratio of the infrared luminosity  $(L_{IR})$ , to the luminosity at 8  $\mu$ m,  $L_8$ , which Elbaz et al. (2011) found to closely correlate with the surface density of MIR and FIR luminosity. In our case, we utilize the CO (J=5-4) line as a proxy for  $L_{\rm IR}$  and the flux in F1800W as  $L_8$ . The uncertainty of IR8 is mainly contributed by the conversion from the luminosity of CO (J=5-4) to between  $L_{\rm IR}$ , which is a small scatter of  $\sim 0.2$  dex. In Fig. 3, the IR8 map peaks at the centre, with a value around 18, which is roughly double the values observed in the surrounding spiral arms, as indicated by the CO contours. While we acknowledge that our measured IR8 may be affected by systematic uncertainties related to CO excitation or temperature variations across different regions of the galaxy, the F1800W data provide a distinct morphological signature: the southeastern spiral arm exhibits a peak flux approximately 80 per cent that of the central region. In contrast, the CO(J=5-4) emission and the dust continuum show more centrally concentrated morphologies with weaker emission in the southeastern arm. This discrepancy

<sup>&</sup>lt;sup>3</sup>Complementary kinematic information and a discussion of the moment 1 and 2 maps, including a modelling attempt, are provided in Appendix B.

suggests that systematic uncertainties alone are unlikely to account for the pronounced *IR8* variations.

We reiterate that there is no evidence suggesting a significant AGN influence. While we cannot completely rule out the presence of a dust-obscured, relatively faint AGN, its impact on both the spectroscopy and SED appears negligible (Section 2) and cannot account for the strong variation in the IR8 map. As shown in previous studies using Spitzer spectroscopy (e.g. Desai et al. 2007), strong dust continuum emission, particularly from compact nuclear regions possibly associated with AGNs, can dilute PAH features and mimic a deficit in spectroscopy. However, if such hidden AGNs were present at the core, we would expect enhanced *F*1800*W* emission due to a mid-IR continuum excess (e.g. Donley et al. 2008; Casey 2012), even if PAH features were suppressed. Instead, we observe the opposite: the *F*1800*W* emission is fainter.

The IR8 enhancement is further supported by our 2D modelling using Sérsic and Spergel profiles. While both models estimate the radius of the central region to be about 0.5 arcsec (4.3 kpc), the Sérsic index derived from the F1800W map ( $n \sim 1$ ) is lower than that from the CO map ( $n \sim 1.7$ ). This suggests that the PAH distribution is more disc-like, while  $L_{\rm IR}$  traced by the CO map has a more concentrated or compact distribution. Therefore, one simple explanation for this elevated IR8 value and disc-like PAH distribution is a deficit in PAH, possibly caused by the destruction of PAH molecules due to the hard radiation field by intense star formation activity in the starburst core (e.g. Draine & Li 2007).

However, some observations find no obvious correlation between the hardness of the radiation field or the emission-line width and IR8 (Inami et al. 2013; Stierwalt et al. 2014). Alternatively, the IR8 difference across various star-forming regions may be linked to dust distribution and temperature, as explained by the concept of 'dust-bounded' regions (Abel et al. 2009; Díaz-Santos et al. 2017). Dust can absorb a fraction of the ionizing radiation, preventing it from reaching the PDR. This absorption results in an increase in dust temperature and a decrease in PAH emission from PDRs. In the relation between IR8 and  $\Sigma_{IR}$ , IR8 remains relatively flat with respect to the radiation field indicator  $\Sigma_{\text{IR}}$  until it reaches a critical density,  $\Sigma_{\rm IR}^{\rm crit} \sim 3-5 \times 10^{10}~L_{\odot}~{\rm kpc}^{-2}$ , as shown in Fig. 4. Beyond this threshold, IR8 increases with  $\Sigma_{IR}$ , a trend confirmed by observations from Elbaz et al. (2018). In PACS-830, we apply three r = 0."3 apertures to measure the  $\Sigma_{IR}$  in the eastern and northern spiral arm and starbursting core from the original CO (J=5-4) map, respectively. We note that, since the northern arm is not robustly detected in CO (J=5-4), we treat the CO luminosity as an upper limit. Consequently, the derived values of IR8 and  $\Sigma_{\rm IR}$  for this region should also be considered upper limits. As depicted in Fig. 4, the result shows that the spiral arm regions are at a lower density ( $\Sigma_{\rm IR} \sim 2 \times 10^{10} \ L_{\odot} \ {\rm kpc}^{-2}$ ), while the core region is of a higher density, at the critical densities ( $\Sigma_{\rm IR} \sim 4 \times 10^{10} \ L_{\odot} \ {\rm kpc}^{-2}$ ), corresponding to a higher IR8. The core density is not exceptionally high – i.e. it does not significantly exceed the critical density – as expected for a moderate starburst (4×MS) with a radius of 0.5 arcsec, as derived from 2D modeling with JWST and ALMA (cf. compact submillimeter sources; Puglisi et al. 2019, 2021; Tan et al. 2024a). However, the density remains sufficient to reveal distinct spatial variations in IR8, consistent with theoretical expectations and prior observations on global properties (Elbaz et al. 2018).

For local galaxies, IR8 also indicates the starburstiness  $R_{\rm SB}$ , i.e. the distance above the MS. Therefore, we examine  $R_{\rm SB}$  in the core region and spiral arms using the SFR (i.e. CO (J=5–4)) and stellar mass maps. The SFR is further inferred from the CO (J=5–4) converted  $L_{\rm TIR}$  map based on the calibration by Hao et al. (2011)

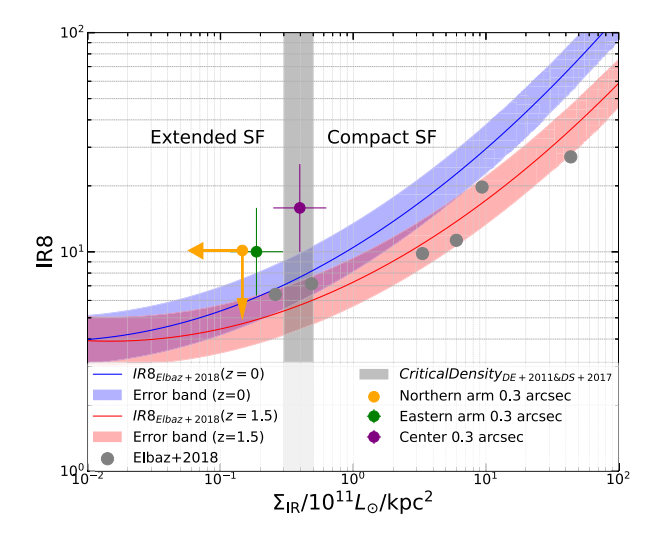


**Figure 4.** IR8 versus  $\Sigma_{IR}$ , with measurements, errorbars (0.2 dex) and upper limits from the eastern and northern spiral arms and central region (0''.3) shown in green, orange, and purple, respectively. The 'critical density' in Elbaz et al. (2011) and Díaz-Santos et al. (2017) is highlighted by the grey shaded region. Two fitted lines at z=0 and z=1.5 from Elbaz et al. (2018) are shown in blue and red, with shaded regions representing a 0.11 dex error range. The grey data points are the starburst galaxies at 1.5 < z < 2.5 from Elbaz et al. (2018).

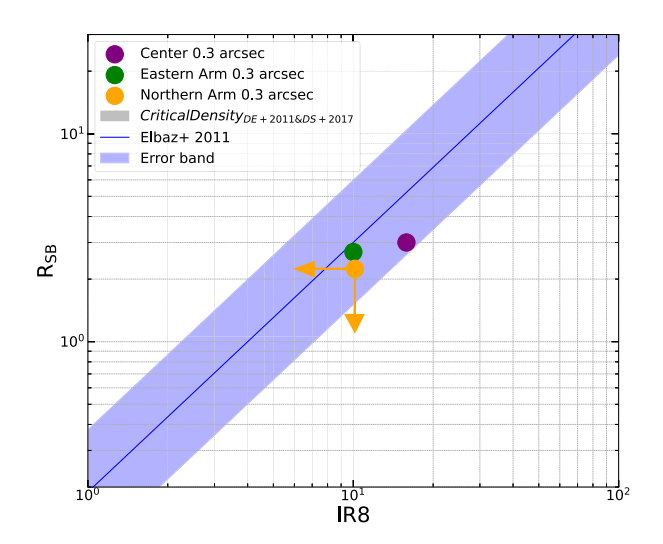


**Figure 5.**  $R_{SB}$  versus IR8, with measurements and upper limits from the eastern and northern spiral arms and central region (0".3) shown in green, orange, and purple, respectively. One fitted line of local galaxies from Elbaz et al. (2011) is shown in blue, with shaded regions representing a 0.3-dex dispersion.

and Murphy et al. (2011). Since the CO (J=5–4) map has a coarser resolution, we first smooth the stellar mass map by doubling the FWHM of its PSF (0.32 arcsec) and then convolve the CO (J=5–4) map to match this new Gaussian-like PSF. We then apply the same apertures as in Fig. 4 to measure the  $R_{\rm SB}$  based on the MS of Speagle et al. (2014). The results well align with the relation in Elbaz et al. (2011), shown in Fig. 5, in contrast to the offset in Fig. 4. This indicates that, for a given  $R_{\rm SB}$ ,  $\Sigma_{\rm IR}$  is lower than expected, suggesting that the star formation mode in this spiral-starburst galaxy may differ from the compact starbursts triggered by major mergers.

### 5 DISCUSSION: FORMATION AND IMPACT OF SUBSTRUCTURES IN PACS-830

In the pre-JWST era, Elmegreen & Elmegreen (2014) suggested a morphological evolutionary path for SFGs, commonly progressing from highly turbulent, gas-rich discs with giant clumps to more ordered spiral galaxies based on HST observations in the rest-frame optical. However, our JWST and ALMA observations of PACS-830 reveal a rare mixed case, in which clumps, spiral arms, and a bulge in formation coexist in a single system, aligning with other emerging JWST results (Kuhn et al. 2024; Kalita et al. 2025b). Notably, we observe a gradual change from a clumpy morphology in the rest-frame UV to a more spiral-like appearance at NIR and MIR wavelengths, hinting that previous conclusions may have been influenced by both high dust attenuation in distant SFGs and the limitations of previous-generation instruments like HST.

In this section, we connect our key findings to existing literature and explore how these substructures emerge and evolve, focusing on the implications of clumps, spiral arms, and bulges for the physical properties across the galaxy. We also highlight the associated SFRs and PAH characteristics as potential diagnostics of the varying conditions within different substructures, thereby providing insights into the interplay of morphological evolution and star formation in distant starburst systems. In particular, we detect a pronounced PAH deficit in the forming bulge, potentially attributable to PAH destruction by the intense radiation field or decreased PDR emissions at the galactic center – an effect likely linked to the enhanced star-forming activity therein sustained by the evolving structure of PACS-830.

### 5.1 A starbursting bulge

Triggered either by violent disc instabilities (VDI; Dekel et al. 2009) or minor-interactions with a neighbouring galaxy (see Section 5.3), the fragmented clumps as well as the spiral arms can contribute to disc instabilities within PACS-830 thus driving bulge formation (see Bournaud 2016, for a review). Over time, the clumps along the spiral arms possibly migrate inward due to gravitational torques and dynamical friction. Additionally, the presence of spiral arms and clumps points to gas inflow, as these non-axisymmetric structures transfer the angular momentum and allow gas to migrate inward. Therefore, the bulge formation may be fueled by a combination of gas and stars, consistent with our observations: the irregular CO shape and the UV/optical clumps spotted in the core region may indicate that the central bulge is growing by both *in situ* and *ex situ* star formation.

The evidence of a deficit in PAH emission may indicate rapid bulge formation due to a higher SFE. Cortzen et al. (2019) report that PAH 6.2  $\mu$ m correlates with CO (J=1–0) from z = 0 – 4 for SMGs, and Shivaei & Boogaard (2024) investigate the relationship between PAH 7.7  $\mu$ m and CO (J=1–0) in 14 MS galaxies at z = 1 – 3, reinforcing that PAH emissions can be used as a proxy for molecular gas mass. A higher IR8 value in PACS-830, therefore, indicates a higher SFE, since SFE is proportional to IR8 (SFE = SFR/M<sub>gas</sub>  $\propto IR8$ ). Such a high SFE in the core region aligns with the rapid bulge formation indicated by the morphology with high global instabilities that may quench the starburst after depleting the central gas rapidly, supporting the inside-out growth scenario. Similar cases are also found in z  $\sim$  2 lensed, massive starburst galaxies at hundreds of parsec scales, but with more centrally depleted molecular gas (Liu et al. 2023, 2024a), possibly linking to different stages of inside-out quenching.

However, it's important to highlight a limitation in our analysis: IR8 is just a colour index, and not a direct comparison of PAH 7.7  $\mu$ m and CO (J=5–4) emissions. Although we infer that the PAH 7.7

 $\mu m$  emission is strong and broad, based on the integrated SED fitting from Liu et al. (2021) and our new MIRI/F1800W photometry (subplot in Fig. 3), we remain uncertain about whether the contribution from the underlying continuum remains consistent. Nevertheless, continuum dilution is unlikely to explain the observed flux deficit at 8  $\mu m$ . To solidify our conclusions, a further spectroscopic study of PACS-830 and a larger sample are necessary.

Regardless of the interpretation, we conclude that this *IR8* enhancement could be a signature of an intense star-forming region, possibly linked to a rapidly growing bulge. Spatially comparing PAH tracers with indicators of star formation (e.g. CO high-*J* transitions or Paschen lines), derived from different physical processes, could be a useful exercise to hunt for SBs hidden in MS (Elbaz et al. 2018) or bulges in formation. This approach is especially promising given the abundant ALMA archival data, the gradually building-up *JWST*/NIRCam WFSS archival data (e.g. COSMOS-3D; Kakiichi et al. 2024) on infrared emission lines and MIRI broadband imagery.

### 5.2 Clumps along the spiral arms

Giant clumps can disrupt the symmetry of the overall mass distribution, thereby enhancing star formation across the disc, potentially seen in the bright CO clump detected in the eastern spiral arm. These clumps are thought to form through disc fragmentation (Elmegreen, Bournaud & Elmegreen 2008), a scenario supported by kinematic observations of clumps in massive gas-rich discs (Genzel et al. 2011). In PACS-830, the gas-to-stellar mass ratio (~1) of the entire galaxy meets the criterion for a gas-rich disc (Silverman et al. 2018b); thus, fragmentation could be triggered by a secular process, i.e. VDI, as expected in Faisst et al. (2025).

However, the most prominent clumps lie along the spiral arms rather than being randomly scattered, hinting that gravitational interactions or other dynamical processes may also play a role (see next section). Despite their seemingly orderly positioning, the clumps vary in size, mass, and SFRs. Interestingly, while the CO (J=5–4) and PAH emissions differ between the eastern and northwestern clumps, their IR8 values remain similar. Of different scales mentioned above, the clumps do not exhibit large differences in their radiation fields or overall starburst activity. This finding aligns with results from local (U)LIRGs in the GOALS sample, where the midinfrared spectra of extended star-forming regions beyond  $\sim$ 1.5 kpc from the nucleus are remarkably homogeneous, and variations in integrated MIR properties primarily reflect the diversity of nuclear conditions (e.g. Díaz-Santos et al. 2011; Stierwalt et al. 2014).

### 5.3 Grand-design spiral arms

PACS-830 has exactly two prominent and symmetric arms along with clumps mostly located on the arms, which resemble a 'grand-design' morphology. Simulations suggest that grand design arms form due to the gravitational interactions with other galaxies instead of VDI, which usually results in multi-armed or flocculent (patchy) morphology (Dobbs et al. 2010). PACS-830 could be a past minor merger as in PACS-819 (Liu et al. 2024b). Or, it is an ongoing mini merger with a neighboring candidate with a similar robust photometric redshift ( $z=1.4764, \sigma_z=0.009$ ) within proximity (<3''). Its redshift is derived from the ZFOURGE survey (Straatman et al. 2016), estimated with the photometry in six filters of the FourStar

 $<sup>^4</sup>$ Another neighbouring galaxy ( $\sim$  8" away) with a similar photo-z does not meet the selection standard in the ZFOURGE catalogue (Straatman et al. 2016).

near-infrared camera on the Magellan telescope, complemented by 25 ancillary photometric filters in the COSMOS field. The colour of the galaxy similar to PACS-830's also indicates that they might be a pair of interacting galaxies.

A stellar mass of  $10^{9.5}\,M_\odot$  and an SFR of  $\sim$ 7 locates it as an MS galaxy. The mass ratio of it and PACS-830 is about 1/30, which is below the threshold for a minor merger (e.g. 1/10 in Bottrell et al. 2024). Bottrell et al. (2024) highlight that mini mergers can trigger small enhancements in SFRs and asymmetries, aligning with the moderate starburst and non-axisymmetric morphology of PACS-830. Given that PACS-830 shows only a moderate offset from the MS, being a factor of 4 above the relation, the interaction of this mini merger could trigger the SFR enhancement and the formation of the grand-design spiral arms. However, this galaxy is undetected in all ALMA maps and shows only a marginal detection with S/N  $\sim$ 4 in F1800W, preventing any further analysis of its PAH and CO emissions.

### 6 FINAL REMARKS

With the help of JWST/MIRI, we can now spatially resolve emissions from critical dust grains - PAHs - in SFGs at cosmic noon. This opens a new window to map star formation in the mid-infrared, particularly for the diverse substructures in these galaxies revealed by JWST/NIRCam. We showcase our analysis of the starburst system PACS-830 at z = 1.463 focusing on its compact nuclear starburst and extended regions using multiwavelength data from HST, JWST, and ALMA. Unlike major-merger-like starbursts, PACS-830 resembles a grand-design spiral galaxy with a bulge-forming nucleus and multiple clumps along its spiral arms, as revealed by NIRCam images. Through pixel-by-pixel SED fitting, we confirm that PACS-830 is indeed a spiral galaxy rather than a multiple major merger suggested by HST images, based on its stellar distribution. This finding downplays the role of major-merger-triggered starbursts in gas-rich galaxies at cosmic noon and favors interaction-induced or VDI-induced scenarios or past minor merger events as in PACS-819 (Liu et al. 2024b).

The CO (J=5–4) and PAH (detected by MIRI/F1800W) emission maps align well with the morphology observed in JWST/NIRCam, tracing star formation in both the central core and the spiral arms. Notably, one of the spiral arms contributes  $\sim$ 20 per cent of the total flux of CO (J=5–4). The comparison of these two maps, along with 2D modeling, reveals a significant PAH deficit in the centre of the galaxy. This deficit is likely due to the destruction of PAHs or decreased PDR emission caused by the intense star formation in the galactic centre. Our findings reveal, for the first time, spatial variations in the  $L_8$  to  $L_{IR}$  ratio, aligning with theoretical predictions and previous global measurements. Consequently, we express caution in using PAHs, particularly MIRI-based PAH indicators, to determine SFRs in a spatially resolved context.

Our findings underscore the importance of high-resolution, multiwavelength observations in revealing the true structure and internal processes of distant galaxies. We also demonstrate that the PAH deficit could serve as a tracer for distant extreme/compact star-forming regions with the help of NIRCam WFSS and MIRI. Further, more detailed studies with enhanced resolution and broader dynamic range will be crucial for understanding the mechanisms driving star formation and galaxy evolution in the early universe.

### **ACKNOWLEDGEMENTS**

We thank the anonymous referee for the insightful comments to improve the manuscript. ZL sincerely thanks Luis C. Ho, Ryota Ikeda, Hanae Inami, Benjamin Magnelli, and Naoki Yoshida for the scientific discussions.

Kavli IPMU was established by World Premier International Research Center Initiative (WPI), MEXT, Japan. ZL is supported by the Global Science Graduate Course (GSGC) program of the University of Tokyo. JS is supported by JSPS KAKENHI (JP22H01262) and the World Premier International Research Center Initiative (WPI), MEXT, Japan. AP is supported by an Anniversary Fellowship at University of Southampton. This research was supported by the Hayakawa Satio Fund awarded by the Astronomical Society of Japan, by NAOJ ALMA Grants No. 320 and 358, and by JSPS Core-to-Core Program (grant number: JPJSCCA20210003).

Some of the data products presented herein were retrieved from the Dawn JWST Archive (DJA). DJA is an initiative of the Cosmic Dawn Center, which is funded by the Danish National Research Foundation under grant no. 140.

### DATA AVAILABILITY

Some of the data presented in this article were obtained from the Mikulski Archive for Space Telescopes (MAST) at the Space Telescope Science Institute. The specific observations analyzed can be accessed via DOI: 10.17909/dny0-c072. This paper makes use of the following ALMA data: ADS/JAO.ALMA#2016.1.01426.S. ALMA is a partnership of ESO (representing its member states), NSF (USA) and NINS (Japan), together with NRC (Canada), MOST and ASIAA (Taiwan), and KASI (Republic of Korea), in cooperation with the Republic of Chile. The Joint ALMA Observatory is operated by ESO, AUI/NRAO, and NAOJ.

### REFERENCES

Abdurro'uf, Lin Y.-T., Wu P.-F., Akiyama M., 2021, ApJS, 254, 15 Abel N. P., Dudley C., Fischer J., Satyapal S., van Hoof P. A. M., 2009, ApJ, 701, 1147

Akins H. B. et al., 2022, ApJ, 934, 64

Alberts S. et al., 2024, ApJ, 976, 224

Bail A. L. et al., 2024, A&A, 688, A53

Battisti A., Shivaei I., Park H. J., Decleir M., Calzetti D., Mathew J., Wisnioski E., da Cunha E., 2025, Publ. Astron. Soc. Aust., 42, e022

Bertin E., 2011, in Evans I. N., Accomazzi A., Mink D. J., Rots A. H., eds, ASP Conf. Ser. Vol. 442, Astronomical Data Analysis Software and Systems XX. Astron. Soc. Pac., San Francisco, p. 435

Boquien M., Burgarella D., Roehlly Y., Buat V., Ciesla L., Corre D., Inoue A. K., Salas H., 2019, A&A, 622, A103

Bottrell C. et al., 2024, MNRAS, 527, 6506

Bournaud F., 2016, in Laurikainen E., Peletier R., Gadotti D., eds, Galactic Bulges. Springer International Publishing, Cham, p. 355, https://doi.org/ 10.1007/978-3-319-19378-6\_13

Brammer G., 2023, grizli, Zenodo

Briggs D. S., 1995, American Astronomical Society Meeting Abstracts, 187, 112.02

Calabrò A. et al., 2024, A&A, 690, A290

Calzetti D., 2013, in Falcón-Barroso J., Knapen J. H., eds, Secular Evolution of Galaxies. Cambridge Univ. Press, Cambridge, p. 419, https://doi.org/ 10.48550/arXiv.1208.2997

Capak P. et al., 2007, ApJS, 172, 99

Cappelluti N. et al., 2009, A&A, 497, 635

Carnall A. C., McLure R. J., Dunlop J. S., Davé R., 2018, MNRAS, 480, 4379

Casey C. M. et al., 2023, ApJ, 954, 31

Casey C. M., 2012, MNRAS, 425, 3094

Chabrier G., 2003, PASP, 115, 763

Chastenet J. et al., 2023, ApJ, 944, L12

Civano F. et al., 2016, ApJ, 819, 62

```
Comrie A. et al., 2021, CARTA: The Cube Analysis and Rendering Tool for
   Astronomy. Zenodo
Condon J. J., Huang Z. P., Yin Q. F., Thuan T. X., 1991, ApJ, 378, 65
Conway J. E., Cornwell T. J., Wilkinson P. N., 1990, MNRAS, 246, 490
Cornwell T. J., 2008, IEEE J. Sel. Top. Signal Proc., 2, 793
Cortzen I. et al., 2019, MNRAS, 482, 1618
Cowie L. L., González-López J., Barger A. J., Bauer F. E., Hsu L. Y., Wang
   W. H., 2018, ApJ, 865, 106
Daddi E. et al., 2007, ApJ, 670, 156
Daddi E. et al., 2015, A&A, 577, A46
Dale D. A. et al., 2023, ApJ, 944, L23
Dekel A. et al., 2009, Nature, 457, 451
Delvecchio I. et al., 2021, A&A, 647, A123
Desai V. et al., 2007, ApJ, 669, 810
Díaz-Santos T. et al., 2011, ApJ, 741, 32
Díaz-Santos T. et al., 2017, ApJ, 846, 32
Ding X. et al., 2020, ApJ, 888, 37
Dobbs C. L., Theis C., Pringle J. E., Bate M. R., 2010, MNRAS, 403, 625
Donley J. L., Rieke G. H., Pérez-González P. G., Barro G., 2008, ApJ, 687,
Draine B. T., 2003, ARA&A, 41, 241
Draine B. T., Li A., 2007, ApJ, 657, 810
Dunlop J. S. et al., 2021, JWST Proposal. Cycle 1, ID. #1837
Egorov O. V. et al., 2023, ApJ, 944, L16
Elbaz D. et al., 2011, A&A, 533, A119
Elbaz D. et al., 2018, A&A, 616, A110
Elmegreen B. G., Bournaud F., Elmegreen D. M., 2008, ApJ, 688, 67
Elmegreen D. M., Elmegreen B. G., 2014, ApJ, 781, 11
Faisst A. L. et al., 2025, ApJ, 980, 204
Ferreira L. et al., 2023, ApJ, 955, 94
Förster Schreiber N. M., Wuyts S., 2020, ARA&A, 58, 661
Franco, M. et al., 2025, preprint (arXiv:2506.03256)
Genzel R. et al., 2011, ApJ, 733, 101
Gillman S. et al., 2024, A&A, 691, A299
Greve T. R. et al., 2014, ApJ, 794, 142
Grogin N. A. et al., 2011, ApJS, 197, 35
Gullberg B. et al., 2019, MNRAS, 490, 4956
Hao C.-N., Kennicutt R. C., Johnson B. D., Calzetti D., Dale D. A., Moustakas
   J., 2011, ApJ, 741, 124
Helou G., Bicay M. D., 1993, ApJ, 415, 93
Hodge J. A. et al., 2016, ApJ, 833, 103
Hodge J. A. et al., 2019, ApJ, 876, 130
Hodge J. A., da Cunha E., 2020, R. Soc. Open Sci., 7, 200556
Ilbert O. et al., 2009, ApJ, 690, 1236
Inami H. et al., 2013, ApJ, 777, 156
Jiménez-Andrade E. F. et al., 2019, A&A, 625, A114
Kakiichi K. et al., 2024, JWST Proposal. Cycle 3, ID. #5893
Kalita B. S. et al., 2025a, MNRAS, 536, 3090
Kalita B. S. et al., 2025b, ApJ, 979, L44
Kalita B. S., Silverman J. D., Daddi E., Bottrell C., Ho L. C., Ding X., Yang
   L., 2024, ApJ, 960, 25
Kalita B. S., Silverman J. D., Daddi E., Mercier W., Ho L. C., Ding X., 2025c,
   MNRAS, 537, 418
Kashino D. et al., 2019, ApJS, 241, 10
Kennedy J., Eberhart R., 1995, in Proceedings of ICNN'95-International
   Conference on Neural Networks, Vol. 4. p. 1942, https://doi.org/10.110
   9/ICNN.1995.488968
```

Kepley A. A., Tsutsumi T., Brogan C. L., Indebetouw R., Yoon I., Mason B.,

Kuhn V., Guo Y., Martin A., Bayless J., Gates E., Puleo A. J., 2024, ApJ, 968,

Lai T. S. Y., Smith J. D. T., Baba S., Spoon H. W. W., Imanishi M., 2020,

Donovan Meyer J., 2020, PASP, 132, 024505

Lacki B. C., Thompson T. A., 2010, ApJ, 717, 196

Koekemoer A. M. et al., 2007, ApJS, 172, 196

Koekemoer A. M. et al., 2011, ApJS, 197, 36

Kokorev V. et al., 2023, A&A, 677, A172

```
M., Nakagawa T., 2024, ApJ, 967, 83
Lai T. S.-Y. et al., 2022, ApJ, 941, L36
Lai T. S.-Y. et al., 2023, ApJ, 957, L26
Lee J. C. et al., 2023, ApJ, 944, L17
Leger A., D'Hendecourt L., Boissel P., Desert F. X., 1989, A&A, 213, 351
Li A., 2020, Nat. Astron., 4, 339
Liu D. et al., 2019, ApJS, 244, 40
Liu D. et al., 2021, ApJ, 909, 56
Liu D. et al., 2023, ApJ, 942, 98
Liu D. et al., 2024a, Nat. Astron., 8, 1181
Liu D., Gao Y., Isaak K., Daddi E., Yang C., Lu N., Werf P. v. d., 2015, ApJ,
Liu Z. et al., 2024b, ApJ, 968, 15
Lyu Y. et al., 2024, A&A 693, A313,
Madau P., Dickinson M., 2014, ARA&A, 52, 415
Magnelli B. et al., 2023, A&A, 678, A83
Marchesi S. et al., 2016, ApJ, 817, 34
McKinney J. et al., 2025, ApJ, 979, 229
McKinney J., Pope A., Armus L., Chary R.-R., Díaz-Santos T., Dickinson M.
   E., Kirkpatrick A., 2020, ApJ, 892, 119
Murphy E. J. et al., 2011, ApJ, 737, 67
Murphy E. J., 2013, ApJ, 777, 58
Pedrini A. et al., 2024, ApJ, 971, 32
Pérez-González P. G. et al., 2024, ApJ, 968, 4
Perrin M. D., Soummer R., Elliott E. M., Lallo M. D., Sivaramakrishnan
   A., 2012, in Clampin M. C., Fazio G. G., MacEwen H. A., Oschmann
   J. M., Jr, eds, Proc. SPIE Conf. Ser. Vol. 8442, Space Telescopes and
   Instrumentation 2012: Optical, Infrared, and Millimeter Wave. SPIE,
    Bellingham, p. 84423D
Polletta M. et al., 2007, ApJ, 663, 81
Polletta M. et al., 2024, A&A, 690, A285
Pope A. et al., 2013, ApJ, 772, 92
Puglisi A. et al., 2019, ApJ, 877, L23
Puglisi A. et al., 2021, MNRAS, 508, 5217
Rizzo F. et al., 2023, A&A, 679, A129
Rodighiero G. et al., 2011, ApJ, 739, L40
Ronayne K. et al., 2024, ApJ, 970, 61
Rujopakarn W. et al., 2023, ApJ, 948, L8
Shivaei I. et al., 2024, A&A, 690, A89
Shivaei I., Boogaard L. A., 2024, A&A, 691, L2
Silverman J. D. et al., 2015, ApJ, 812, L23
Silverman J. D. et al., 2018a, ApJ, 867, 92
Silverman J. D. et al., 2018b, ApJ, 868, 75
Smolčić V. et al., 2017, A&A, 602, A1
Solomon P. M., Bout P. A. V., 2005, ARA&A, 43, 677
Speagle J. S., Steinhardt C. L., Capak P. L., Silverman J. D., 2014, ApJS,
   214, 15
Spergel D. N., 2010, ApJS, 191, 58
Spilker J. S. et al., 2023, Nature, 618, 708
Stierwalt S. et al., 2013, ApJS, 206, 1
Stierwalt S. et al., 2014, ApJ, 790, 124
Straatman C. M. S. et al., 2016, ApJ, 830, 51
Tacconi L. J. et al., 2013, ApJ, 768, 74
Tacconi L. J., Genzel R., Sternberg A., 2020, ARA&A, 58, 157
Tan Q.-H. et al., 2024a, Nature, 636, 69
Tan Q.-H. et al., 2024b, A&A, 684, A23
Tanaka T. S. et al., 2025, ApJ, 979, 215
Teodoro E. M. D., Fraternali F., 2015, MNRAS, 451, 3021
Tielens A. G. G. M., 2008, ARA&A, 46, 289
Valentino F. et al., 2020, A&A, 641, A155
Zhang L., Ho L. C., Li A., 2022, ApJ, 939, 22
```

Lai T. S. Y., Smith J. D. T., Peeters E., Spoon H. W. W., Baba S., Imanishi

L15

ApJ, 905, 55

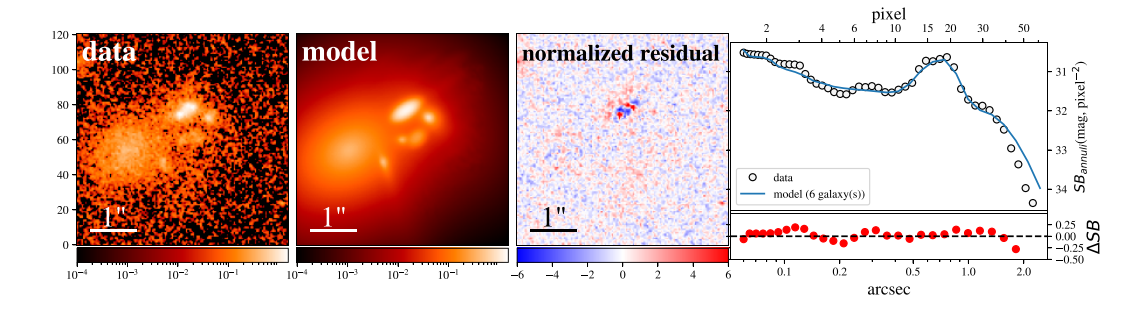


Figure A1. Sérsic model fit to the 2D emission in F606W using Galight with panels as follows from left to right: science image, model image, residual image (data-model/ $\sigma$ ), and 1D surface brightness profile.

# APPENDIX A: AN EXAMPLE OF THE FOREGROUND GALAXY SUBTRACTION USING SÉRSIC MODELLING WITH GALIGHT

As depicted in Fig. 1, PACS-830 shows diverse substructures across different wavelengths, making it difficult to apply the same components of models in all the bands, while the foreground galaxy circled by the blue dash line in Fig. 1 remains relatively consistent in terms of the shape from F435W to F150W. Therefore, we start from F814W, where the two galaxies have the best contrast, to model the foreground galaxy and sub-components of PACS-830 simultaneously. Afterward, we fix the position and Sérsic shape of the foreground galaxy when fitting in the other bands. We set the fitting result of F606W as an example of the modeling and foreground subtraction.

### APPENDIX B: MOMENT 1 AND 2 MAPS

We generated the moment 1 (velocity field) and moment 2 (velocity dispersion) maps from the CO (J=5–4) data cube binned to 40 km s<sup>-1</sup> channels (Fig. B1). To ensure reliable measurements, we applied a mask that retains only those pixels with at least five consecutive

channels having S/N above 5. For pixels adjacent to high-S/N regions, we relaxed the threshold to S/N > 3.

The moment 1 map reveals a disc-like velocity field, consistent with rotation, and even shows hints of a spiral feature. The moment 2 map also aligns with expectations for a rotating disc, displaying elevated velocity dispersion in the central region. However, we note that the current spatial resolution and signal-to-noise ratio limit a more detailed interpretation. In particular, while the central enhancement in dispersion is qualitatively consistent with the presence of a bulge, it is also consistent with expectations for a disc without requiring a bulge component, unless a proper model comparison is made.

We also attempted to model the CO kinematics using the 3DBarolo code (Teodoro & Fraternali 2015). While the residual maps were generally acceptable, the fitted dispersion values carried large uncertainties and exceeded the measured values. This may reflect limitations in the modeling or a relatively low intrinsic velocity dispersion ( $\lesssim 10~\rm km~s^{-1}$ ). Furthermore, our spectral binning (40 km s<sup>-1</sup>) is significantly larger than the expected dispersion, making the results unreliable. For these reasons, we decided not to include quantitative 3DBarolo results in either the main text or the appendix.

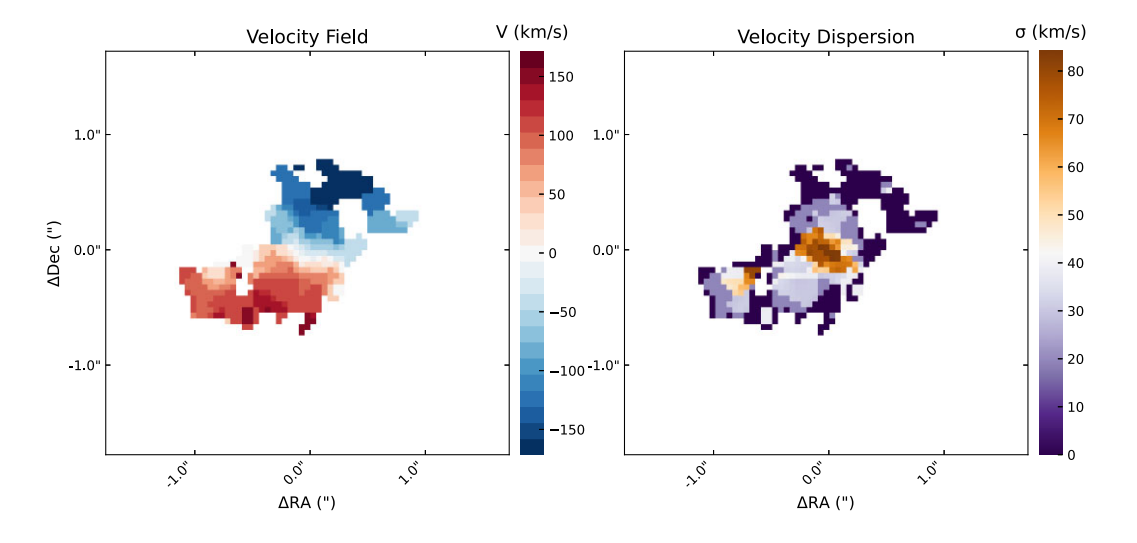


**Figure B1.** Moment 1 and 2 map of CO (J=5-4).

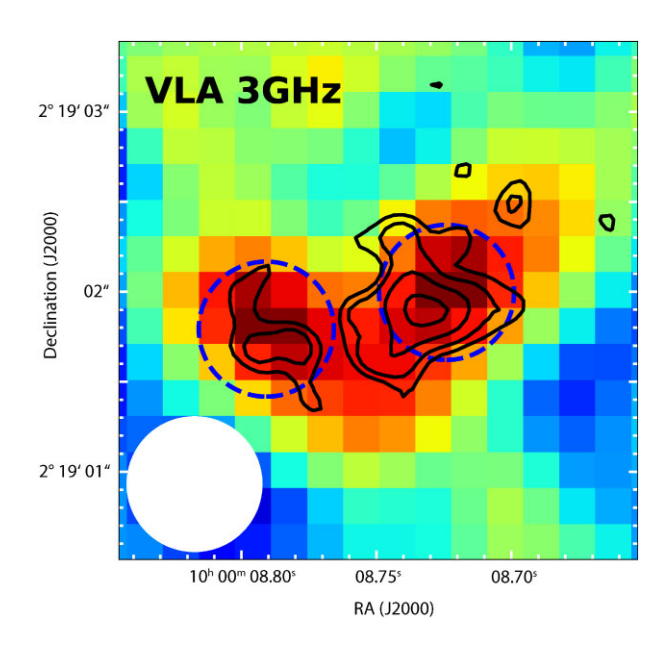


**Figure C1.** VLA 3 GHz observation. The dashed circles represent the apertures of one beam size that we use to measure the flux ratio between the spiral arm and the core region. The solid contours are generated from CO (J=5-4) emissions.

### APPENDIX C: VLA 3 GHZ OBSERVATION

We retrieve the VLA 3 GHz observations from the VLA-COSMOS 3 GHz Large Project (Smolčić et al. 2017) via the COSMOS cutout tool. The beam size is  $0''.75 \times 0''.75$ . To our surprise, VLA captures two peaks equivalent in strength at the locations of the spiral arm and starbursting core, respectively. We measure the physical distance between the two peaks and the foreground galaxy to the galactic centre of PACS-830 in F606W and confirm the eastern peak in VLA 3 GHz is not from the foreground galaxy. As the peaks are slightly smaller than  $5\sigma_{\rm rms}$  ( $\sigma_{\rm rms}=2.39\,\mu$  Jy beam<sup>-1</sup>), they are not included in the VLA-COSMOS catalogue and the related paper on the radio sizes of SFGs (Smolčić et al. 2017; Jiménez-Andrade et al. 2019). Therefore, we will not overinterpret the data and only discuss the flux ratio ( $\sim$ 1:1) in two different structures measured by two aperture photometries (r = 0''.375, one beam size; locations shown in Fig. C1). As a region with a high  $\Sigma_{SFR}$  and stellar mass density, the starburst core is expected to be of a lower IR-to-radio luminosity ratio  $q_{\rm IR}$  (for definition see equation 1 in Delvecchio et al. 2021) than the spiral arm region. Yet, the fact is vice versa. This could be explained by a flatter radio spectrum due to free-free absorption (e.g. Condon et al. 1991; Murphy 2013) or a shorter cosmic ray scale heights (e.g. Helou & Bicay 1993; Lacki & Thompson 2010). Another explanation for the high radio emission in the spiral arm is that it could be a tidally disrupted galaxy hiding an AGN. Yet, this explanation cannot address the enhanced radio emission between the two peaks.

A more certain investigation is beyond the scope of the data we currently have. We expect the next-generation radio telescope will solve the mystery of the missing radio flux in the starburst core of PACS-830.

<sup>5</sup>COSMOS Cutouts.

- <sup>1</sup> Kavli Institute for the Physics and Mathematics of the Universe (Kavli IPMU, WPI), UTIAS, The University of Tokyo, Kashiwa, Chiba 277-8583, Japan
- <sup>2</sup>Department of Astronomy, School of Science, The University of Tokyo, 7-3-1 Hongo, Bunkyo, Tokyo 113-0033, Japan
- <sup>3</sup>Center for Data-Driven Discovery, Kavli IPMU (WPI), UTIAS, The University of Tokyo, Kashiwa, Chiba 277-8583, Japan
- <sup>4</sup>Université Paris-Saclay, Université Paris Cité, CEA, CNRS, AIM, F-91191 Gif-sur-Yvette, France
- <sup>5</sup>Center for Astrophysical Sciences, Department of Physics & Astronomy, Johns Hopkins University, Baltimore, MD 21218, USA
- <sup>6</sup>Kavli Institute for Astronomy and Astrophysics, Peking University, Beijing 100871, P. R. China
- <sup>7</sup>School of Physics and Astronomy, University of Southampton, Highfield SO17 1BJ, UK
- <sup>8</sup>Department of Astronomy, School of Physics, Peking University, Beijing 100871, China
- <sup>9</sup>Istituto Nazionale di Astrofisica (INAF), Osservatorio Astronomico di Padova, Vicolo dell'Osservatorio 5, I-35122 Padova, Italy
- <sup>10</sup>National Astronomical Observatory of Japan, 2-21-1 Osawa, Mitaka, Tokyo 181-8588, Japan
- <sup>11</sup>Cosmic Dawn Center (DAWN), Denmark
- <sup>12</sup>Niels Bohr Institute, University of Copenhagen, Jagtvej 128, DK-2200 Copenhagen N. Denmark
- <sup>13</sup>Laboratory for Multiwavelength Astrophysics, School of Physics and Astronomy, Rochester Institute of Technology, 84 Lomb Memorial Drive, Rochester, NY 14623, USA
- <sup>14</sup>Purple Mountain Observatory, Chinese Academy of Sciences, 10 Yuanhua Road, Nanjing 210023, China
- <sup>15</sup>Centro de Astrobiología (CAB), CSIC-INTA, Ctra. de Ajalvir km 4, Torrejón de Ardoz, E-28850 Madrid, Spain
- <sup>16</sup>Department of Astronomy, The University of Texas at Austin, 2515 Speedway Boulevard Stop C1400, Austin, TX 78712, USA
- <sup>17</sup>School of Physics and Technology, Wuhan University, Wuhan 430072, China
- <sup>18</sup>Caltech/IPAC,1200 E. California Blvd., Pasadena, CA 91125, USA
- <sup>19</sup>Astrophysics Research, University of Hertfordshire, Hatfield AL10 9AB, UK
- <sup>20</sup>Space Telescope Science Institute, 3700 San Martin Drive, Baltimore, MD 21218, USA
- <sup>21</sup>NASA Goddard Space Flight Center, Code 662, Greenbelt, MD 20771, IISA
- <sup>22</sup>DTU Space, Technical University of Denmark, Elektrovej, Building 328, DK-2800 Kgs. Lyngby, Denmark
- <sup>23</sup>Department of Computer Science, Aalto University, PO Box 15400, FI-00076 Espoo, Finland
- <sup>24</sup>Department of Physics, University of Helsinki, PO Box 64, FI-00014 Helsinki, Finland
- <sup>25</sup>Institut d'Astrophysique de Paris, UMR 7095, CNRS, and Sorbonne Université, 98 bis boulevard Arago, F-75014 Paris, France
- <sup>26</sup> Jet Propulsion Laboratory, California Institute of Technology, 4800 Oak Grove Drive, Pasadena, CA 91001, USA
- <sup>27</sup>Department of Astronomy and Astrophysics, University of California, Santa Cruz, 1156 High Street, Santa Cruz, CA 95064, USA
- <sup>28</sup>Department of Physics and Astronomy, Università degli Studi di Padova, Vicolo dell'Osservatorio 3, I-35122 Padova, Italy
- <sup>29</sup> Department of Physics, Faculty of Science, Chulalongkorn University, 254 Phayathai Road, Pathumwan, Bangkok 10330, Thailand
- <sup>30</sup>National Astronomical Research Institute of Thailand, 260 Moo 4, T. Donkaew, A. Maerim, Chiangmai 50180, Thailand
- <sup>31</sup>Astronomy Centre, University of Sussex, Falmer, Brighton BN1 9QH, UK
- <sup>32</sup>Department of Physics, University of Miami, Coral Gables, FL 33124, USA

This paper has been typeset from a TEX/LATEX file prepared by the author.